

Article

On Oxidation Resistance Mechanisms at 1273 K of Tungsten-Based Alloys Containing Chromium and Yttria

Felix Klein ^{1,*} , Tobias Wegener ¹ , Andrey Litnovsky ¹ , Marcin Rasinski ¹, Xiaoyue Tan ^{1,2}, Janina Schmitz ^{1,3}, Christian Linsmeier ¹ , Jan Willem Coenen ¹, Hongchu Du ⁴ , Joachim Mayer ⁴  and Uwe Breuer ⁵ 

¹ Forschungszentrum Jülich GmbH, Institut für Energie- und Klimaforschung—Plasmaphysik, Partner of the Trilateral Euregio Cluster (TEC), 52425 Jülich, Germany; wegener.tobias@gmail.com (T.W.); a.litnovsky@fz-juelich.de (A.L.); m.rasinski@fz-juelich.de (M.R.); jscltan2012221@163.com (X.T.);

jan.schmitz@fz-juelich.de (J.S.); ch.linsmeier@fz-juelich.de (C.L.); j.w.coenen@fz-juelich.de (J.W.C.)

² School of Materials Science and Engineering, Hefei University of Technology, Hefei 230009, China

³ Department of Applied Physics, Ghent University, 9000 Ghent, Belgium

⁴ Forschungszentrum Jülich GmbH, Ernst Ruska-Centrum, 52425 Jülich, Germany; h.du@fz-juelich.de (H.D.); mayer@gfe.rwth-aachen.de (J.M.)

⁵ Forschungszentrum Jülich GmbH, Central Institute for Engineering, Electronics and Analytics ZEA-3, 52425 Jülich, Germany; uwe.breuer@fz-juelich.de

* Correspondence: fe.klein@fz-juelich.de

Received: 5 May 2018; Accepted: 15 June 2018; Published: 26 June 2018



Abstract: Tungsten (W) is currently deemed the main candidate for the plasma-facing armor material of the first wall of future fusion reactors, such as DEMO. Advantages of W include a high melting point, high thermal conductivity, low tritium retention, and low erosion yield. However, as an accident to occur, air ingress into the vacuum vessel could occur and the temperature of the first wall could reach 1200 K to 1450 K due to nuclear decay heat. In the absence of cooling, the temperature remains in that range for several weeks. At these temperatures, the radioactive tungsten oxidizes and then volatilizes. Smart W alloys are therefore being developed. Smart alloys are supposed to preserve properties of W during plasma operation while suppressing tungsten oxide formation in case of an accident. This study focuses on investigations of thin film smart alloys produced by magnetron sputtering. These alloys provide an idealistic system with a homogeneous distribution of the elements W, chromium (Cr), and yttrium (Y) on an atomic scale. The recommended composition is W with 12 weight % of Cr and 0.5 weight % of Y. Passivation and a suppression of WO₃ sublimation is shown. For the first time, the mechanisms yielding the improved oxidation resistance are analyzed in detail. A protective Cr₂O₃ layer forms at the surface. The different stages of the oxidation processes up to the failure of the protective function are analyzed for the first time. Using ¹⁸O as a tracer, it is shown for the first time that the oxide growth occurs at the surface of the protective oxide. The Cr is continuously replenished from the bulk of the sample, including the Cr-rich phase which forms during exposure at 1273 K. A homogenous distribution of yttria within the W-matrix, which is preserved during oxidation, is a peculiarity of the analyzed alloy. Further, an Y-enriched nucleation site is found at the interface between metal and oxide. This nucleation sites are deemed to be crucial for the improved oxidation resistance.

Keywords: W-based alloys; W-Cr-Y alloys; oxidation resistance; DEMO; magnetron thin films; diffusion; isotope tracer; yttria; yttrium

1. Introduction

Fusion reactions are the power source of the sun. The process relies on a nuclear reaction, fusing nuclei to convert mass into kinetic energy. Fusion research aims at employing this process in a fusion power plant. Deuterium and tritium in a plasma are required as fuel [1].

The plasma is magnetically confined in the vacuum vessel of a fusion reactor; the loads on the first wall of future fusion power plants such as DEMO will be much higher compared to current experimental devices: heat and particle loads of around 0.5 MW m^{-2} and $2 \times 10^{21} \text{ m}^{-2} \text{ s}^{-1}$ are foreseen to reach the first wall of the vessel [2]. Further, an average neutron wall load of 2.0 to 2.4 MW m^{-2} is expected [3]. Therefore, the material selection for the first wall is a crucial issue. One field of research comprises the extreme conditions of regular operation [2,4], another field represents worst-case accidental scenarios [5]. The requirements imposed from both fields have to be combined to develop advanced materials [6].

Tungsten (W) is currently the main candidate for plasma-facing armor material [7,8]. Advantages of W include a high melting point, high thermal conductivity, low tritium retention, and low erosion yield. The activity induced by the neutron irradiation of W in DEMO decays to the hands-on level of $10 \mu\text{Sv h}^{-1}$ within 100 years [9]. Thus, the W is recyclable within 100 years, which is the same situation as for the vacuum vessel [10]. It leaves two properties that should be improved—the mechanical and the oxidation properties. The mechanical properties are the subject of intensive research addressed elsewhere [11–14].

This study assumes the so-called Loss-of-Coolant-Accident (LOCA) with simultaneous air ingress. In such a case, the plasma switches off by itself due to impurity influx, no chain-reaction is possible [3]. However, the first wall is activated by neutrons during operation and heats up due to nuclear decay heat in the absence of cooling. Intensive modeling work has been performed by Maisonnier et al. [3], who find that the temperature can peak at 1200 K to 1450 K and remain in that range for several months. The temperature heavily depends on the size, fusion power, material composition, and cooling system of the power plant. In the case of a LOCA, W oxidizes to WO_3 and then sublimates [15]. For a typical 1000 m^2 surface of the first wall, several hundreds of kg per week of radioactive W would sublime at 1273 K, and even more at higher temperatures [16]. This sublimation is severely hazardous for the environment and a major drawback of pure W as an armor material in DEMO. Therefore, the oxidation properties are crucial and solutions must be found to generate passive safety for a fusion power plant.

Smart alloys could be a solution. A 2 mm thick layer of smart alloy could be fixed onto the structural material as the plasma-facing armor material. The concept of smart alloys is to adapt their properties to the environment. Smart alloys concept comprises the advantageous properties of W during plasma operation [17,18] coupled with suppressed tungsten oxide formation during an accident [5]: during normal operation, the plasma preferentially sputters the alloying elements with a lower mass compared to W [19], leaving a depleted zone of almost pure W as plasma-facing surface. When a LOCA occurs, the alloy must passively adapt to the new environment. The W in the depleted zone oxidizes and sublimates. Assuming a 10 nm depletion zone [20] and a 1000 m^2 surface of the first wall, this depletion zone corresponds to only 0.2 kg of W. Then the alloying elements form a protective oxide layer on the surface, which suppresses further oxidation of W and consequently also the sublimation of WO_3 [18].

A material with good oxidation resistance requires a passivation agent to form a protective oxide layer. Different passivation agents are considered: aluminum (Al), silicon (Si), and chromium (Cr) [21]. Al is not suitable for a fusion power plant as it forms long-lived radioactive isotopes under neutron irradiation [9]. Si forms stable silicides with W, constraining the mechanical workability of the alloy [5,22]. Cr is the remaining element capable of forming a protective layer. A small amount of Y is found to be crucial for the improved oxidation resistance [16,23], in comparison to binary W-Cr or W-Cr-Ti alloys, which were investigated in other studies [5].

In particular the adherence of the protective oxide scale is improved in the presence of Y [24]. The fact that small amounts of active elements, such as Y, substantially improve the adherence of oxide

scales, was discovered in 1937 [25]. Since then Y has been added to various alloys and studies on the role of Y have been conducted [23,24,26–32].

Typically Y segregates at the grain boundaries as Y_2O_3 and $YCrO_4$ [33,34]. One effect attributed to Y is a decreased grain size of alloys due to grain boundary pinning [26]. Smaller grains increase the oxide plasticity as long as no macroscopic yttrium-containing phases form [26], prevents the direct initiation of scale failure and contributes to an improved adherence [26]. Further, Y can tie up impurities such as S, C, or P, which otherwise destabilize the oxide layer [24].

Y is also found at the alloy-oxide interface [24,28]. There it may result in two more effects. First, Y provides additional nucleation sites, which yield a faster formation of a more homogeneous and closed Cr_2O_3 film in the beginning of the oxidation process [27,29,30]. This closed oxide film is beneficial for the further oxidation and the overall oxidation is much slower for long oxidation times. Second, it can cause the formation of so-called pegs, local spots where the surface oxide layer grows deeper into the alloy, which increase the adherence by 'clamping' the oxide and the alloy together [24,27,31].

However, none of the studies, looking at the mechanisms of how Y works, analyzed W-Cr-Y alloys. Previous works on W-Cr-Y alloys featured an elemental composition scan by systematically varying the concentration of Cr and Y. These studies resulted in the optimized alloy composition of W-12Cr-0.6Y [16]. Here and in the following the numbers before the element represent the concentration in weight (wt.) %. For example W-12Cr-0.6Y means that the alloy contains 87.4 wt. % W, 12 wt. % Cr, and 0.6 wt. % Y. Further, the performance of smart alloys in humid environment [35], and the performance under plasma exposure [36] were investigated. Currently, there is a lack on the understanding of the detailed mechanisms yielding the oxidation resistance of smart alloys. In this paper these mechanisms are addressed in detail for the first time.

This paper has the following structure:

- An overview of the employed experimental methods and the preparation of the alloys is given.
- The prepared alloys are pre-characterized.
- The changes during oxidation are analyzed, first on a macroscopic scale by measuring the mass change, then on a microscopic scale by imaging the microstructure. This analysis investigates the protective oxide layer, discusses the main failure mechanism of the oxide, and predicts a lifetime.
- Further details on the microscopic properties are investigated: the diffusion processes yielding the formation of the protective oxide are analyzed and the phase formation, including its consequences, is studied.
- The distribution of alloying elements is analyzed on a nano-scale. A particular focus is on Y which is not detected in measurements on a microscopic scale.

2. Experimental Methods

2.1. Analysis Techniques

The weight change during oxidation is measured using the thermogravimetric analyzer TAG-16/18 from Setaram, 69300 Caluire, France. The samples hang, attached to platinum wires, in a tube with a diameter of 2.2 cm in a constant, laminar gas flow of 10 mL min^{-1} . The time, temperature, and atmosphere during the experiment can be controlled. Diffusion processes are measured by changing the isotope abundance of O_2 .

The microstructure is analyzed using the Carl Zeiss Crossbeam 540 electron microscope manufactured by Carl Zeiss Microscopy GmbH, 07745 Jena, Germany. The following modules are used in this work: Scanning Electron Microscopy (SEM) for imaging, Focused Ion Beam (FIB) nanomanipulation to create cross sections, a gas-injection system for deposition of a protective platinum coating before cutting, and Energy-Dispersive X-ray spectroscopy (EDX) (Oxford Instruments NanoAnalysis, High Wycombe, England, U.K.) to determine different elements. Imaging on a nano-scale is done by Scanning Transmission Electron Microscopy (STEM) using the FEI Titan 80-300 STEM at the Ernst Ruska-Centre [37].

Depth-resolved composition profiles are measured by Secondary Ion Mass Spectrometry (SIMS) using a ToF-SIMS IV facility by ION-TOF GmbH, 48149 Münster, Germany. SIMS measurements in this work use cesium (Cs) ions with an energy of 2 keV and a current of 140 μA on an area of $9 \times 10^4 \mu\text{m}^2$ for sputtering a crater. A bismuth Bi_3^+ beam with an energy of 25 keV and a current of 1 nA on an area of $\sim 5 \times 10^3 \mu\text{m}^2$ progressively generates secondary ions to analyze the bottom of the crater.

The oxygen content of the samples is determined using sputter X-ray Photoelectron Spectroscopy (XPS). The sample is inserted in vacuum (10^{-8} Pa), the surface is cleaned using an argon beam, and the clean surface is irradiated with an Al K_{α} X-ray source.

The lattice structure of the alloy is measured by X-ray diffraction (XRD) using the D8 Discover from Bruker AXS GmbH, 76187 Karlsruhe, Germany. During the experiment, the X-ray source, a copper X-ray tube, and the silicon strip detector are continuously rotated to obtain a diffractogram.

2.2. Sample Preparation

Thin smart alloy films prepared by deposition in a magnetron sputter device, manufactured by PREVAC, 44362 Rogow, Poland, are used as samples for the investigations in this work. In a magnetron sputter device, material is ejected from a metallic target and deposited on a substrate. In the system used for this work, the pressure is reduced to below 10^{-4} Pa before every process to minimize contamination. Then argon, which is used as sputtering projectile, is introduced. The flow rate is adjusted so that the pressure in the vacuum vessel stabilizes at 0.6 Pa. The sputtering process uses an electrical and a magnetic field near the target area. A negative voltage in the range of 100–500 V is applied, which accelerates argon ions towards the target. These ions release atoms from the target, which then deposit on a circular sapphire substrate with a diameter of 1.2 cm.

Multiple targets with a diameter of 7.6 cm each are focused onto one spot, are connected to independent power sources and operated in parallel. The parallel operation allows alloying. The elemental composition of the film is controlled by changing the power supplied to each target. The more power is supplied to a target of a certain element, the higher is the sputtering rate and the higher the concentration of that element in the alloy. The W-(12 to 13) Cr-(0.4 to 1) Y samples are obtained with a power of 500 W for W, 270 W for Cr, and 170 W to 240 W for Y. The chosen deposition time ranges from 85 min to 180 min. No further treatments, such as roughening, polishing, annealing, or chemical reagents, are applied after deposition before oxidation.

3. Sample Pre-Characterization

The weight of the deposited thin films within one sputtering process is 6 mg to 12 mg with a fluctuation below 2% within one deposition. The thickness, measured on a cross section after a FIB cut, is 3–8 μm .

After deposition of the samples, an O content of ~ 8 atomic % is found. Y oxidizes at room temperature, the standard free energy of the reaction of Y to Y_2O_3 is -1.2 MJ mol^{-1} [38]. The oxygen content in the sample and the standard free energy indicate that all yttrium in the alloy has reacted to yttria. In comparison W-10Cr-2Ti alloys compacted by pressureless sintering and subsequent HIPing achieved an O content of ~ 2 atomic % [39]. The O content of samples produced by magnetron sputtering could be reduced by pumping a better vacuum, currently 10^{-4} Pa is reached. However, the potential benefits are not clear and the present study analyzes the samples which can be produced with the present setup.

The density of the thin films is calculated from the surface area of the substrate, the thickness of the film, and its mass. A relative density of 92 to 97% of the theoretical density is achieved. Figure 1a shows the micro-structure of the sputtered films before further treatment. The images are taken using electron microscopy on the surface and on a cross section. No phase separation or local segregation of specific elements is detected, the atomically dispersed yttria is not resolved, and the grain size is around 0.2 μm . In addition, the SIMS measurement shown in Figure 1b shows a constant distribution of elements within the alloy, only the O content is slightly increased within the first 0.2 μm . Different elements

are detected with a different sensitivity, therefore the counts cannot be compared to get the relative composition.

XRD diffractograms are acquired to confirm that the sputtered films have a W-like lattice structure. The results are depicted in Figure 2. Alloyed samples exhibit a characteristic shape, all main W peaks are visible. For example, the (211) peak at $2\Theta = 73.1^\circ$ in Figure 2 has a FWHM of 1.8° . In comparison, pure W prepared by magnetron sputtering exhibits the (211) peak at $2\Theta = 73.2^\circ$ and has a FWHM of 0.3° . Alloying causes the increased peak width indicating that there are more strain and defects in the alloy as compared to the pure W. No peaks at the position where Cr peaks are expected are found in the alloys.

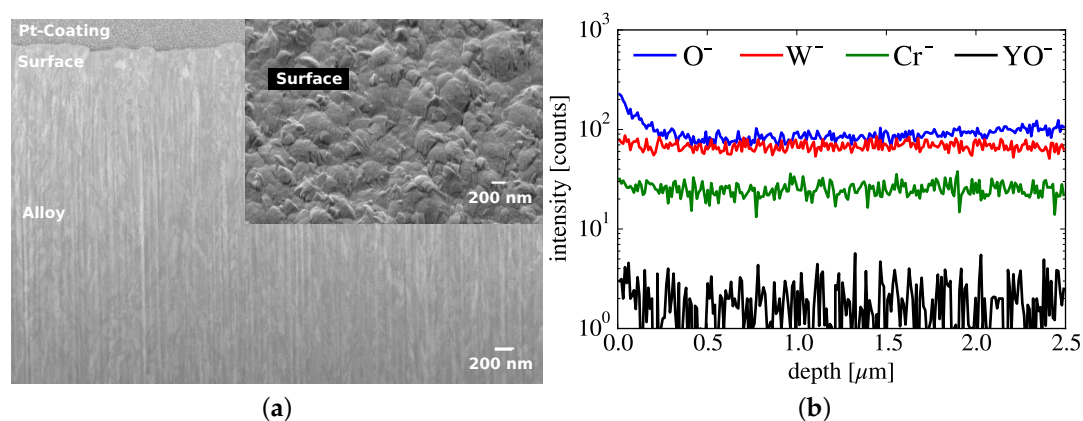


Figure 1. (a) Electron microscopy images of an W-13Cr-1Y alloy as deposited, exemplary for the alloys used in this work. The inset shows the surface, the cross-sectional view depicts the protective platinum (Pt) coating and the alloy; (b) SIMS profile of an exemplary W-12Cr-0.5Y alloy as deposited.

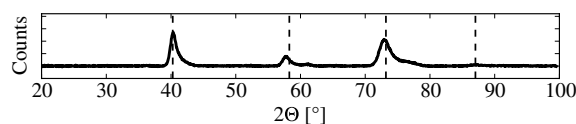


Figure 2. XRD measurement of an W-12Cr-0.5Y alloy as deposited, exemplary for the alloys used in this work. The black, dashed lines indicate the expected peak-positions for W based on the database [40].

Table 1. Positions of peaks in the XRD shown in Figure 2 in comparison to the peaks of pure W.

	(110)-Plane	(200)-Plane	(211)-Plane	(220)-Plane
Expected peak for pure W [40]	40.265°	58.276°	73.198°	87.024°
Measured smart alloy peak	40.4°	57.8°	73.1°	87.1°

As seen in the cross section shown in Figure 1a, a crystal structure with elongated submicron grains forms. This structure is due to a defined growth direction during sputtering, and is in agreement with literature expectations for the selected process parameters [41]. The crystal is therefore anisotropic and the relative intensities of peaks in the XRD should not be compared to literature of isotropic materials.

The peak shift in the XRD can be translated to a change in lattice constant of tungsten, $a_W = 3.1648 \text{ \AA}$ [40]. Based on the position of the four main peaks indicated in Figure 2 and given in Table 1, the lattice constant can be calculated to

$$a = (1.002 \pm 0.004) \times a_W \quad (1)$$

Thus, the lattice constant of the W matrix changes less than 1% compared to that of pure W. In comparison, Vegard's law can be used to estimate the lattice constant a_{Vegard} assuming a perfect substitutional solid:

$$a_{\text{Vegard}} = x_A \times a_{\text{Cr}} + (1 - x_A) \times a_W = 0.97 \times a_W \quad (2)$$

where $x_A = 12 \text{ wt. \%} = 32 \text{ atom \%}$ is the Cr concentration and $a_{\text{Cr}} = 2.91 \text{ \AA}$ the Cr lattice constant [42]. The contradiction of Equations (1) and (2) means that Vegard's law is not valid in this specific case.

The magnetron films used in this study, provide an idealistic system with a homogeneous distribution of the alloying elements on an atomic scale. Due to this homogenous distribution, thin films are ideal for fundamental studies on understanding the properties of the material, which is the topic of this paper.

4. Macroscopic and Microscopic Changes During Oxidation

4.1. Macroscopic Changes: Mass Change

In this section, the mass change of the films deposited by magnetron sputtering is measured at a temperature of 1273 K at atmospheric pressure, with 20 kPa O_2 and 80 kPa Ar partial pressure. In a first step the sublimation rates of pure oxides are investigated: one sample contains pure W, another sample contains Cr and Y. Then they are oxidized at 1273 K in Ar- O_2 until no more mass gain is observed and the samples are completely oxidized. These samples provide reference rates for the sublimation of different oxides. The result is plotted in Figure 3a. The mass of the Cr-Y-O sample is almost constant with time, the measured rate is $2 \times 10^{-7} \text{ mg cm}^{-2} \text{ s}^{-1} \cong 0.9 \mu\text{g h}^{-1}$. In contrast, a mass loss with a rate of $7 \times 10^{-6} \text{ mg cm}^{-2} \text{ s}^{-1}$ is measured on the WO_3 sample, see Figure 3a. The mass loss is caused by sublimation. This rate corresponds to a surface recession of 0.01 nm s^{-1} .

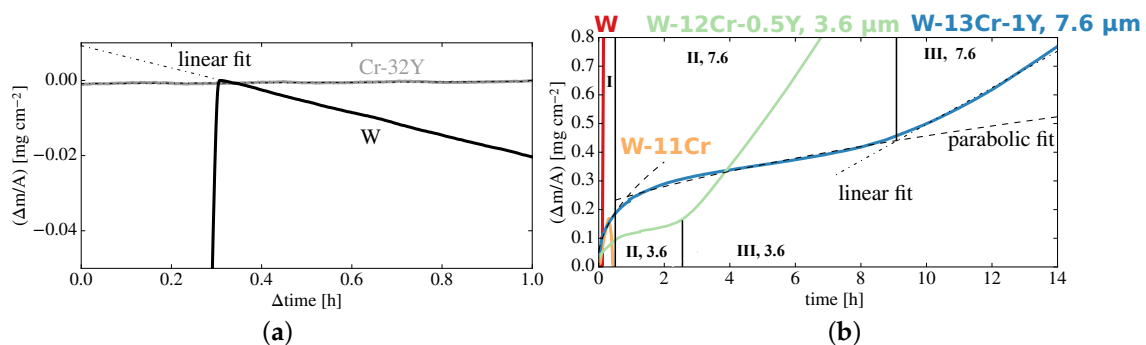


Figure 3. Mass change of thin films as a function of time. The samples were exposed to a temperature of 1273 K at 20 kPa O_2 and 80 kPa Ar partial pressure. (a) shows CrY-oxide and a W-oxide; (b) Shows smart alloys. Oxidation stages I-III are labeled, the numbers 3.6 and 7.6 refer to the sample thickness of 3.6 μm and 7.6 μm , respectively.

In the next step, mass gain due to oxidation is investigated. The mass change with respect to time of W, W-Cr, and W-Cr-Y is shown in Figure 3b. Pure W exhibits fast linear mass gain at a rate of $6 \times 10^{-3} \text{ mg cm}^{-2} \text{ s}^{-1}$. Binary W-Cr alloys show parabolic behavior with a rate of $4 \times 10^{-5} \text{ mg}^2 \text{ cm}^{-4} \text{ s}^{-1}$, reducing to a minimum gradient of $1 \times 10^{-4} \text{ mg cm}^{-2} \text{ s}^{-1}$. After 15 min the film detaches from the substrate, indicating complete failure of the protective function. The oxidation process of the W-Cr-Y films can be separated into three stages:

1. Stage I lasts 0.5 h, the 7.6 μm thick sample exhibits a parabolic oxidation rate of $2 \times 10^{-5} \text{ mg}^2 \text{ cm}^{-4} \text{ s}^{-1}$. In comparison, the rate for the 3.6 μm thick sample with the optimized composition is 4 times lower.

- Stage II exhibits a parabolic oxidation rate reduced to $5 \times 10^{-6} \text{ mg}^2 \text{ cm}^{-4} \text{ s}^{-1}$ for the $7.6 \mu\text{m}$ thick sample. A gradient as low as $4 \times 10^{-6} \text{ mg cm}^{-2} \text{ s}^{-1}$ is reached. Stage II ends after 9 h; for a thinner sample, with a thickness of $3.6 \mu\text{m}$ stage II lasted only 2.3 h under identical conditions despite the optimized composition and a lower oxidation rate of $2 \times 10^{-6} \text{ mg}^2 \text{ cm}^{-4} \text{ s}^{-1}$.
- Stage III follows for samples of either thickness. An increased mass gain with a linear rate of $5 \times 10^{-5} \text{ mg cm}^{-2} \text{ s}^{-1}$ or $2 \times 10^{-5} \text{ mg cm}^{-2} \text{ s}^{-1}$ is measured for the $3.6 \mu\text{m}$ and $7.6 \mu\text{m}$ thick samples, respectively.

4.2. Microscopic Changes: Microstructure

To gain a deeper understanding of these stages, identical W-12Cr-0.5Y samples with a thickness of $3.6 \mu\text{m}$ samples are analyzed after different oxidation times. The times are chosen in order to obtain samples from the different stages in the oxidation process. Results of cross section viewing in the SEM are depicted in Figure 4; a layer of Pt is deposited onto the surface before cutting to avoid damage of the surface by sputtering.

The W-C12r-0.5Y sample shown in Figure 4a is oxidized for 10 min and corresponds to stage one. A total mass increase of 0.08 mg is detected. The surface oxide layer has a thickness of $0.15 \pm 0.04 \mu\text{m}$ with a typical grain size below $0.1 \mu\text{m}$. The alloy beneath the oxide has a thickness of $3.30 \pm 0.03 \mu\text{m}$. The darker spots within the alloy constitute about 2% of the imaged area in Figure 4a. The darker spots are identified as chromium oxide by EDX - thus internal oxidation starts. The EDX line scan overlaid with the SEM confirms the layered structure: protective oxide on top of the alloy. The scan is conducted with an electron energy of 5 kV, thus the main peaks of Cr at 0.57 keV and O at 0.52 keV overlap to one combined peak.

The W-C12r-0.5Y sample shown in Figure 4b is oxidized for 1.25 h. It corresponds to oxidation stage II. A total mass increase of 0.18 mg is detected. The surface oxide layer thickness increases to $0.23 \pm 0.04 \mu\text{m}$ with a typical grain size of around $0.1 \mu\text{m}$. The thickness of the alloy beneath the oxide is $3.31 \pm 0.03 \mu\text{m}$, this is constant as compared to Figure 4a. Graphical analysis yields, that the internal oxidation fills about 8% of the imaged area in Figure 4b. According to EDX, the Cr concentration in the alloy reduced from initially 12 wt. % to 8 wt. %. The SIMS profiles are drawn into the electron image, see Figure 4b. Within the oxide, mostly Cr and O signal is measured by SIMS whereas the W signal vanishes. Within the alloy, W, Cr, and O are measured. The W signal remains constant throughout the rest of the film whereas according to the SIMS signals Cr and O gradually decrease from depth $0.5 \mu\text{m}$ to $2.0 \mu\text{m}$ and remain constant afterwards.

For comparison to W-Cr-Y, the binary W-11Cr is also analyzed. A hilly surface, with local delamination and a grain size of around $0.1 \mu\text{m}$ is found. The intact region of the W-Cr alloy is analyzed using SIMS and cross section viewing using SEM and EDX, see Figure 4d. A layered structure is found. On the surface there is a layer of Cr_2O_3 with a thickness of $h_s = 0.19 \pm 0.04 \mu\text{m}$, partially coated by a few nm WO_3 . Below is a layer of mixed tungsten-chromium oxide with a thickness $h_m = 0.64 \pm 0.09 \mu\text{m}$ and visible pores. The alloy starts below the mixed oxide. In the first $\approx 0.3 \mu\text{m}$, some pores, but little internal oxides are visible. In the central region of the film, the alloy is interspersed with chromium oxide, identified by EDX, while in the last few hundreds of nanometers only the alloy is visible. From the SIMS profile, Figure 4d, this finding is confirmed. Moreover, the chromium signal exhibits a minimum around the interface of the tungsten-chromium oxide with the alloy. The oxygen signal gradually decreases from a maximum at the surface to a minimum at the interface to the substrate.

The $3.6 \mu\text{m}$ thin W-C12r-0.5Y sample in Figure 4c is oxidized for 8 h. It belongs to oxidation stage III. A total mass increase of 1.12 mg is recorded. On the surface two different oxides are stacked. Using an EDX line scan at an acceleration voltage of 5 keV, overlaid in Figure 4c, it is shown that there is a top layer of tungsten oxide with a thickness of around $0.2 \pm 0.1 \mu\text{m}$. It has grains of a few 100 nm. Below, there is a Cr_2O_3 layer with a thickness of around $0.4 \pm 0.1 \mu\text{m}$. Within the Cr_2O_3 layer, small white spots are visible, which are identified as W by EDX. An example is marked in Figure 4c.

In addition, an increasing number of pores opening up at the interface of the alloy with the Cr_2O_3 and inside the oxides is observed. The thickness of the alloy beneath the oxide increases to $3.54 \pm 0.05 \mu\text{m}$ due to the volume expansion of the internal oxide. The internal oxidation reaches down to the substrate and covers an area of about 20%. According to EDX using an acceleration voltage of 10 keV and the K_α -line of Cr, the Cr content in the alloy is 7 wt. %.

The yttria is not resolved in any of the measurements shown in this section. This result indicates a very fine distribution of the yttria. Section 6 presents STEM measurements, targeting to resolve the yttria.

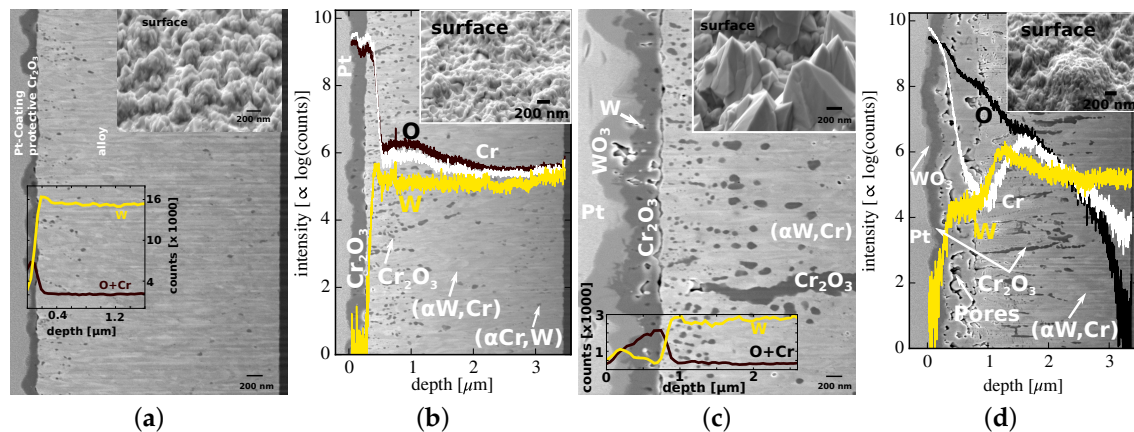


Figure 4. Electron microscopy images of cross sections and surface images in the inset. The ternary W-12Cr-0.5Y alloy is shown in (a–c), whereas (d) is the binary W-11Cr alloy. They are exposed to a temperature of 1273 K at 20 kPa O_2 and 80 kPa Ar partial pressure: (a) for 10 min; (b) for 75 min; (c) for 8 h; (d) for 15 min. In (b,d) the corresponding SIMS profile and in (a,c) the corresponding EDX-line scans in the region of the box are overlaid with the electron image.

4.3. Evaluation of the Oxidation Performance

To start with, the discussion focuses on the first oxidation stage observed in Figure 3b. In oxidation stage I only Cr_2O_3 , no WO_x , forms as confirmed by SEM/EDX measurements (Figure 4a). The Gibbs free energy at a temperature $T = 1273 \text{ K}$ of Cr_2O_3 $\Delta G_{\text{Cr}_2\text{O}_3}^{T=1273 \text{ K}} = -5.3 \times 10^2 \text{ kJ}/(\text{mol O}_2)$ [43] is much lower than for WO_3 where $\Delta G_{\text{WO}_3}^{T=1273 \text{ K}} = -3.6 \times 10^2 \text{ kJ}/(\text{mol O}_2)$ [43]. Thus, Cr is more affine to O_2 than W and sufficient Cr (and yttria—see Section 6) present at the surface can suppress oxidation of W. Any Y_2O_3 is not reduced as the Gibbs free energy $\Delta G_{\text{Y}_2\text{O}_3}^{T=1273 \text{ K}} = -1.4 \times 10^3 \text{ kJ}/(\text{mol O}_2)$ is much lower compared to the Gibbs energies of Cr and W [43].

As seen in Figure 4, the oxide layer in stage one, with a thickness below $0.2 \mu\text{m}$, is thinner than in later stages. However, as shown in Figure 3b, the difference in mass gain between stage I and II is larger than the parabolic rate law predicts. In fact, the mass gain in stage I follows its own parabolic rate law with $k_p = 2 \times 10^{-5} \text{ mg}^2 \text{ cm}^{-4} \text{ s}^{-1}$. One hypothesis is, that the differences between oxidation stage I and the other stages are related to the adsorption of O at the surface and to the grain size of the oxide layer. It is smaller than in later stages but at the same order of magnitude as the oxide layer thickness. Thus, the edges of certain oxide grains provide a short diffusion path for ions. Another hypothesis is, that yttria influences the process by offering additional nucleation sites, the concept of nucleation sites is observed and discussed in Section 6. Within the first ~ 30 min, it is crucial that a closed protective oxide layer forms to achieve passivation in later stages, which is observed.

There are three key questions for application in a fusion power plant, a first estimation can be given:

1. Is oxidation of tungsten suppressed?
2. Does the chromium oxide sublime/evaporate?

3. How long can the material last?

Is Oxidation of Tungsten Suppressed?

The first question, whether oxidation of W is suppressed, is straightforward to answer: the SEM images in Figure 4 show that no WO_x forms in stages I and II. It means, that at any time there is sufficient Cr supply to suppress the oxidation of W. A local minimum in the Cr concentration, as observed in the binary W-Cr alloy (see Figure 4d), indicates that Cr diffusion is too slow to level the Cr concentration and the Cr supply to the surface is interrupted. In the W-Cr-Y alloy the Cr diffusion is sufficiently fast to avoid such an interruption and the partial oxygen pressure below the Cr_2O_3 layer is kept sufficiently low to avoid W oxidation: at 1273 K W oxidizes at a partial oxygen pressure of 10^{-9} Pa whereas Cr requires only 10^{-17} Pa [38]. This understanding, a continuously growing, protective Cr_2O_3 layer on top of the alloy is supported by the fact, that the thickness of the alloy beneath the oxide remains constant throughout stages I and II (Figure 4a,b).

Does the Chromium Oxide Sublimate/Evaporate?

The second question, whether chromium oxide sublimates, is answered in Figure 3a. W-32Y oxidizes and potentially sublimates simultaneously. The mass gain due to oxidation dominates. At some point it is fully oxidized and the mass gain due to oxidation is zero. After that point the mass change from sublimation is measured. The measured mass change of Cr-32Y-oxide is beyond the accuracy of the used thermobalance as it corresponds to a total mass increase below $1 \mu\text{g h}^{-1}$. In summary, it can be claimed, that no mass change is measured and the sublimation/evaporation rates of chromium and yttrium oxides in Ar + O_2 atmosphere at 1273 K are below the detection limits. This finding is in agreement with literature. For instance at 1373 K (100 K higher than the temperature investigated in our study) a sublimation rate of $2.5 \times 10^{-7} \text{ mg cm}^{-2} \text{ s}^{-1}$ was found [44]. In contrast WO_3 sublimates significantly as shown in Figure 3a. This sublimation rate can only be measured on pure WO_3 , not on a mixture of W and WO_3 as the mass loss due to sublimation of WO_3 is ~1000 times slower than the mass gain due to oxidation of W.

How Long Can the Material Last?

To answer this question, the properties of stages II and III must be understood. This understanding includes the reason for the transition to stage III. The EDX shown in Figure 4c proves the presence of WO_x starting from stage III. The Cr available for replenishing the protective layer decreases since Cr_2O_3 forms and the required Cr can only be provided by the alloy. The amount of Cr required to cause the mass gain at the end of stage II can be calculated using the assumption that mass gain is caused by the formation of Cr_2O_3 only. A new Cr concentration $c_{\text{new}}^{\text{Cr}}$ is found by subtracting the amount of Cr which has reacted to Cr_2O_3 from the total amount of Cr in the alloy. This calculation yields $c_{\text{new}}^{\text{Cr}} \approx 5 \text{ wt. \%}$ in the alloy at the end of stage II. However, edge effects were neglected. Edge effects feature oxidation of W at the edge of the sample due to weaker adhesion of the protective layer at the edge. Including the oxidized W into the calculations explained above yields that the transition to stage III occurs at around $c_{\text{new}}^{\text{Cr}} = 8 \text{ wt. \%}$ metallic Cr in the alloy. Thus, the calculation agrees with the results from EDX. Previously [16] it is presented that effective passivation requires around 0.6 wt. % of Y and more than 8 wt. % of Cr. Thus, W starts to oxidize in stage III (as seen in Figure 4c) in addition to the remaining Cr and the mass-change rate increases in stage III of the oxidation process (as seen in Figure 3b). Thus, the amount of material determines the achievable passivation time.

After these considerations, we discuss oxidation stage III depicted in Figure 3b. In stage III also W oxidizes, since the amount of remaining Cr is not sufficient to suppress this process. The WO_3 forms on top of the previously formed Cr_2O_3 layer, as seen in Figure 4c. That means W diffuses through the oxide layer. This finding is also confirmed by the small W spots, which form within the Cr_2O_3 layer. W^{6+} ions have a mass of 184 u and an ionic radius of 74 pm [45], whereas Cr^{3+} and O^{2-} ions have a mass of 52 u and 16 u with ionic radii of 75.5 pm and 126 pm, respectively [45]. Thus, W diffusing

through the oxide layer is geometrically plausible. As the W diffuses outwards, the observed voids form at the interface of the alloy with the Cr_2O_3 , shown in Figure 4c. We assume that this process occurs the slower the thicker the protective oxide layer is. As the 7.6 μm thick sample has thicker oxide layer than the 3.6 μm thick sample at the failure point, the thick sample oxidizes slower in oxidation stage III.

There are two consequences of the protection failure: first, the protective layer is weakened and more O can penetrate causing more internal oxidation. Second, the WO_3 sublimates on the surface, thus stage III must not be reached in any accidental scenario of a fusion power plant.

With these considerations, we return to the third question, of how long the material would last. It is now obvious that it essentially reads, how long stage II lasts, as stage III must not be reached in any accidental scenario in a fusion power plant. Thin films with an initial thickness of 3.6 μm lasted for 2.3 h in this study. However, in a real fusion power plant the first W-based wall will be around 2 mm thick and the durability heavily depends on the thickness. To quantify this dependence, the diffusion behavior of Cr must be studied.

In the following a homogeneous Cr concentration in the metal during oxidation is assumed: Cr diffusion is sufficiently fast so that the concentration of Cr decreases monotonously with oxidation time. Experimental evidences are presented and discussed in Section 5. This assumption is used in combination with the measured parabolic oxidation constant $k_p = 5 \times 10^{-6} \text{ mg}^2 \text{ cm}^{-4} \text{ s}^{-1}$, to estimate the effect of the alloy thickness: as discussed earlier in this section, the Cr concentration decreases from 12 wt. % to 8 wt. %. This estimation yields 0.5 h and 2.2 h in stage II for the 3.6 μm and 7.6 μm thick samples, respectively. Thus it underestimates the performance, as 2.3 h and 9 h are measured. This underestimation is expected, because k_p also includes the mass gain of fast oxidation at the edges of the sample so that the k_p of an infinite sample would be even smaller. Nevertheless, the model predicts that a 2 mm component remains for more than 10 years in the second oxidation stage in dry, O_2 -containing atmosphere at 1273 K. In comparison, the critical temperature would be maintained for a few months in the accidental scenario of DEMO [3]. Therefore, it can be predicted that the material withstands an accident where the temperature of the first wall rises to 1273 K in air. This prediction implies the assumption that the oxidation resistance is not degraded by the exposure to the plasma of the power plant as argued in Section 1. First experimental evidences are presented in ref. [46].

5. Microscopic Properties

5.1. On the Growth Direction of the Oxide

As the formation of the oxide is crucial for oxidation protection, development of the alloys requires an understanding of the oxide formation process. Thus, a W-12Cr-0.6Y alloy is oxidized in a dedicated experiment, consisting of two parts: part 1 starts with 65 min oxidation at 1273 K in natural $\text{O}_2 + \text{Ar}$. Then the natural O_2 is changed to isotope $^{18}\text{O}_2$ for 11 min so that post-analysis can provide time-resolved information on the O_2 diffusion. $^{16}\text{O}_2$ still remains in the furnace but is gradually flushed out, thus the ratio of $^{18}\text{O}/^{16}\text{O}$ changes. After analysis at room temperature part 2 is performed: the sample is oxidized again at 1273 K in natural $\text{O}_2 + \text{Ar}$ for 20 min. The oxygen-isotope content in dependence of the depth is measured after each part using SIMS.

It is not possible to measure both isotopes ^{16}O and ^{18}O within the oxide layer and the alloy: using a low current, ^{16}O can be measured throughout the entire sample, but ^{18}O is below the detection limit in the alloy. Using a high current, ^{18}O can be measured throughout the entire sample, but ^{16}O is saturated in the oxide layer. However, the molecules $^{16}\text{O}_2$ and $^{16}\text{O}^{18}\text{O}$ can be measured in the oxide using a high current. As the different O-isotopes are chemically identical, the ^{18}O isotope abundance is determined using the ratio of $^{16}\text{O}^{18}\text{O}/^{16}\text{O}_2$ molecules in the oxide, which is marked with the gray background in Figure 5. In the alloy beneath the oxide, the ratio of $^{16}\text{O}/^{18}\text{O}$ ions is used to calculate the ^{18}O isotope abundance, Figure 5.

The following description of Figure 5 starts with part 1 of the experiment at the surface of the sample, depth = 0 μm : ^{18}O exhibits a maximum abundance at the surface of the oxide layer and gradually decreases with higher depth. At a depth of around 1 μm , the ^{18}O abundance slightly increases again to a local maximum at a depth of around 2 μm . An increase of abundance does not necessarily mean an increase of the absolute amount of O. The increase is only around 0.1 %, thus part 2 is described before drawing conclusions.

The description of part 2 of the experiment, Figure 5, starts again at the surface of the sample: there the ^{18}O abundance is close to the natural abundance. Then it increases steeply to a maximum in the oxide layer at ~ 0.1 μm below the surface. Afterwards, it decreases with depth, steeper than in part 1. A low ^{18}O isotope abundance is found throughout the remaining oxide and within the first ~ 0.5 μm of the alloy. At a depth of around 2 μm a broad local maximum of the ^{18}O isotope abundance forms. This maximum is at the same depth as the increase after part one. Thus, a fraction of O must have diffused to a depth of 2 μm within 0.5 h.

After part 1 of the experiment, see Figure 5, the ^{18}O inserted during the last minutes of the experiment is found at the surface of the protective oxide layer. After part 2 new Cr_2O_3 forms at the surface, on top of an ^{18}O -enriched Cr_2O_3 . These results prove that the oxide layer grows primarily at the surface in direct contact with the oxidizing atmosphere. Thus, Cr diffusion towards the surface is dominant over the inward diffusion of O. This finding is important as the Pilling–Bedworth ratio of Cr is 2 [24] and the new Cr_2O_3 can expand freely. Growth at the interface between metal and oxide could cause spallation of the oxide scale. Further, the ^{18}O peak at the surface narrows, see Figure 5. That means, some O diffuses through the protective layer to form the internal oxide. This is O which is not bound to Cr and immobile at room temperature—cooling after part 1 is performed at a rate of 40 K min^{-1} . In part 2, this ^{18}O , not bound to Cr, diffuses to the maximum depth of the internal oxide where new internal oxides can form and a local maximum in the ^{18}O abundance appears at about 2 μm below the surface. That means, that the internal oxide remains immobile once formed and that O must diffuse into the alloy to form internal oxides.

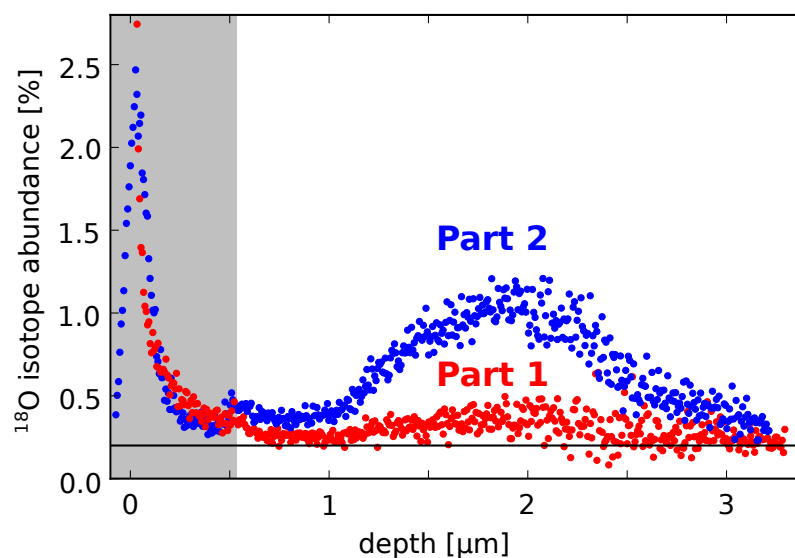


Figure 5. Part 1: ^{18}O isotope abundance after oxidation of W-12Cr-0.6Y at 1273 K for 65 min in $\text{Ar} + ^{16}\text{O}_2$ atmosphere followed by 11 min with increased ^{18}O abundance. Part 2: continued oxidation of the sample from part 1 at 1273 K for 20 min in $\text{Ar} + ^{16}\text{O}_2$ atmosphere. The depth to which the Cr_2O_3 layer extends is marked in gray. The natural abundance of 0.2 % ^{18}O is marked by the black line [47].

5.2. On Diffusion of Cr and Phase Formation

From the previous section it is known that the protective oxide grows due to the diffusion of Cr. Thus, the Cr diffusion and the resulting distributions of Cr should be analyzed in more detail. In Figure 6a the Cr distribution within the sample shown in Figure 4b is investigated using EDX with an electron energy of 5 keV. The Cr_2O_3 layer on the surface (region A), where a high brightness indicates a high Cr signal, is defined as depth = 0 μm . Inside the alloy (region B) the Cr signal appears rather constant, only a few spots with increased Cr signal, which can be correlated with the internal oxidation, are visible. The profile of the Cr concentration with depth, inset of Figure 6a, is calculated by integrating the signal intensity over x at a specific depth. A Cr concentration of ~ 8 wt. % in the alloy (region B) is detected using an electron energy of 10 keV.

The thicker the sample, the longer it can be oxidized without depleting the Cr reservoir. It is easier to resolve Cr diffusion after long times at elevated temperatures since Cr has more time to diffuse. Therefore, a $7.6 \mu\text{m}$ thick sample is oxidized for 6 h. The sample, Figure 6b, is in oxidation stage II and features a $0.9 \pm 0.2 \mu\text{m}$ thick oxide layer (region A). EDX and SIMS show a Cr_2O_3 layer followed by the alloy with a relatively constant Cr concentration. The formation of Cr-rich and -poor phases is observed (region C). Within the first few μm of the alloy (region B), pores with the size of 50–100 nm are found. Grains from the Cr-rich phase form porosity once their Cr is consumed.

The phase formation probably changes the mechanical properties and the sputtering properties. However, this is not relevant for application as temperatures above 1200 K are reached only in a major accident after which the power plant will not be restarted. An operation temperature of only 900 K is foreseen [2]. The lower temperature causes diffusion processes to be exponentially slower. In the W-13Cr-1Y sample shown in Figure 6 the phase formation and the porosity do not degrade the oxidation resistance. However, one needs to investigate the consequences after longer oxidation times, which is not possible with thin films due to Cr depletion.

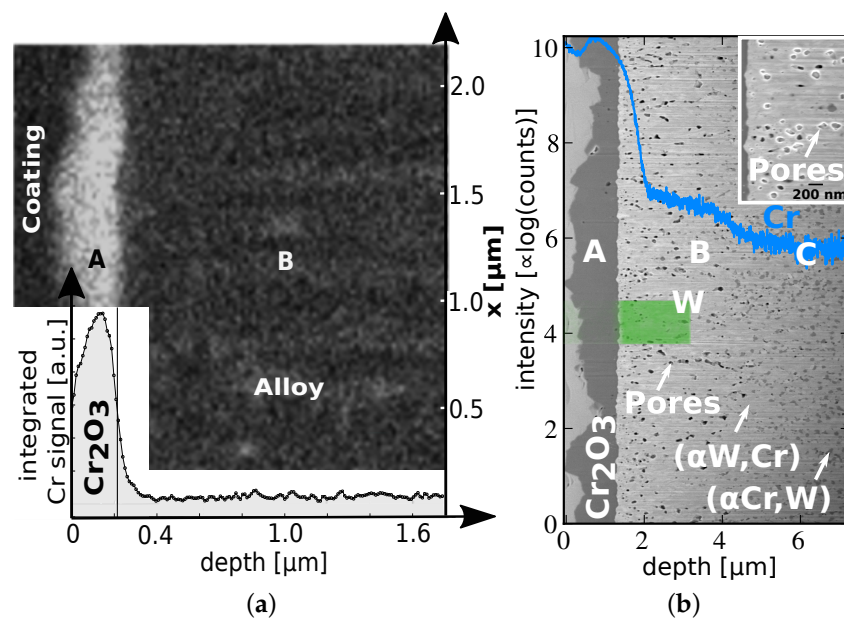


Figure 6. (a) Map of the chromium concentration measured with EDX on the W-12Cr-0.5Y sample shown in Figure 4b. The intensity signal was based on the Cr $L_{\alpha,1,2}$ lines. The inset is derived by integration of the intensity over x . The regions of the oxide and the alloy are labeled A and B, respectively; (b) Electron microscopy image of a cross section of a thick ($7.6 \mu\text{m}$) W-13Cr-1Y alloy. It was exposed to a temperature of 1273 K at 20 kPa O_2 and 80 kPa Ar partial pressure for 6 h. Overlaid are the corresponding Cr-profile measured using SIMS and an EDX map of W based on the W M_{α} line. The image in the inset has an increased magnification and shows the pores more clearly.

A dedicated experiment (see Figure 7b) separates the effects of phase formation and of oxidation: W-Cr-Y samples with a thickness of 3.6 μm are heated in Ar atmosphere at 1273 K for 75 min and 180 min. The Ar atmosphere during baking is obtained by nine times flushing with 99.9999 % pure Ar followed by evacuation of the furnace to a minimum pressure of 0.8 Pa, labeled as Ar_a, or 0.6 Pa, labeled as Ar_b. Thus, the residual oxygen level is different in Ar_a and Ar_b. The residual oxygen causes slow mass gain due to oxidation during baking. The SEM image in Figure 7a shows the formation of a Cr-rich phase after the annealing step. The darker regions belong to the (αCr , W) phase, whereas the brighter regions are identified as (αW , Cr) phase. The samples are then oxidized at 1273 K in 20 kPa O₂ and 80 kPa Ar partial pressure. The mass gain characteristics of the alloy without heating prior to oxidation are explained in Section 4.1, here it is shown as a reference. The mass gain due to oxidation of the alloys after baking includes the mass gain during baking. The starting time of the curves is shifted so that the curves start on the reference measurement. After 1.25 h and after 3 h of heating, the three stages of oxidation are still observed and no clear effect on the oxidation behavior is found. In all cases the transition to oxidation stage 3 occurs at a mass gain above $\sim 0.15 \text{ mg cm}^{-2}$ —this part is shaded in Figure 7b.

This behavior suggests, that the oxidation resistance in stages I and II is not driven by the phase formation and confirms that the Cr dissolved in the (αCr , W) phase remains available for the formation of the protective oxide layer. This finding is important for future alloy developments: it is not crucial to find ways to avoid phase formation on a nano-scale. That means, a homogeneously distributed (αCr , W) phase, with clusters not larger than a few tens of nm (as seen in Figure 7a), does not degrade the oxidation resistance.

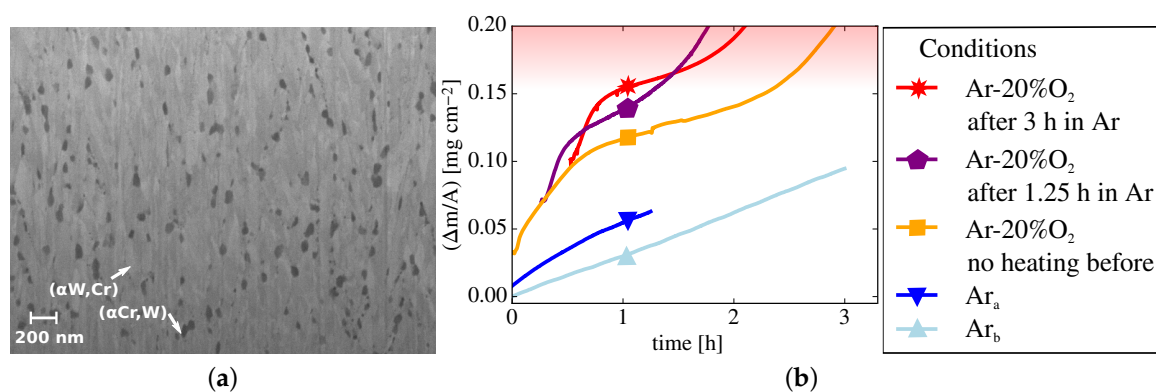


Figure 7. (a) Microstructure of a W-12Cr-0.5Y alloy after 3 h annealing in Ar; (b) Mass change with respect to time of W-12Cr-0.5Y samples at 1273 K. The oxidation behavior after 0 min, 75 min, and 180 min annealing in Ar is shown.

At the end of Section 4.3 it is predicted that a 2 mm thick W-Cr-Y component can withstand a LOCA. This prediction is based on an interpolation to larger thickness and relies on a continuous supply of Cr to the protective layer. In the following the experimental evidences for sufficiently fast diffusion of Cr are discussed. The EDX measurement on the cross section of the same sample after a FIB cut, Figure 6a, shows constant Cr concentration with depth. However, there are measurement uncertainties: first, the sample is tilted during the measurement, so that electrons penetrating just below the surface oxide layer may also give signal from the surface Cr₂O₃ layer. Second, the investigated chromium L_{α} line at 0.57 keV [48] and oxygen K_{α} line at 0.52 keV [48] overlap.

Therefore, the Cr concentration with depth is also measured by SIMS, Figures 4b and 6b. For the understanding of the SIMS measurement it is crucial to know that matrix effects increase the intensity of the secondary Cr ions when sputtering CrO_x instead of pure Cr [49]. Therefore, the increased intensity in the first $\sim 2 \mu\text{m}$ (region B) may not be due to higher Cr content, but due to a higher fraction of Cr₂O₃. Thus, from the SIMS measurement a constant Cr level can only be resolved starting from a depth of

~2 μm (region C), where Cr and O signals are found to be constant with depth. Despite the different oxidation time, the Cr profile remains similar for the samples shown in Figures 4b and 6b. In both cases, any significant concentration gradient in region B near the protective oxide scale should also induce a gradient near the substrate, region C, where the SIMS signal is constant. Therefore, a constant Cr concentration with depth in the entire alloy is confirmed.

This constant concentration of Cr is crucial to provide a constant Cr supply to the protective Cr_2O_3 layer, which suppresses the formation of WO_3 . The diffusion coefficient D of Cr impurities in W at a temperature $T = 2084$ K is given by

$$D(T = 2084 \text{ K}) = D_0 \times \exp\left(-\frac{Q}{k_B T}\right) = 1.74 \times 10^{-18} \text{ m}^2 \text{ s}^{-1} \quad (3)$$

with the Boltzmann constant k_B , the pre-exponential factor $D_0 = 0.89 \times 10^{-4} \text{ m}^2 \text{ s}^{-1}$, and the diffusion energy $Q = 5.669 \text{ eV}$ valid in the temperature range from 2084 K to 2658 K [50]. As the diffusion coefficient is proportional to the mean square displacement of the atoms, it can be used to estimate an expected root mean squared displacement s in three dimensions during the oxidation time $t = 75 \text{ min}$. It can be found that $s = \sqrt{6Dt} = 2 \times 10^{-7} \text{ m}$. The displacement in the experiment in this work should be much smaller due to the lower temperature of 1273 K instead of the 2084 K assumed in the calculations. The real displacement can be estimated from geometrical considerations: the depth d from which the Cr must originate can be calculated using the mass of Cr in the scale $m_{\text{Cr}} = 0.09 \text{ mg}$, the sample area $A = 1.1 \text{ cm}^2$, the measured alloy density $\rho = 15 \text{ g cm}^{-2}$, and the Cr concentration $c = 12 \text{ wt. \%}$.

$$d = \frac{m_{\text{Cr}}}{A\rho c} = 5 \times 10^{-7} \text{ m} \quad (4)$$

This depth is the minimum displacement of Cr. Thus, Cr diffuses much faster than expected from ref. [50]. The submicron grain size and the nano-structure of the alloy, which is investigated in the Section 6, is responsible for this behavior.

In the following the influence of the grain size on the diffusion of Cr is estimated. In the absence of data for a W-Cr-Y alloy, the volume diffusion coefficient $D_V = 6.1 \times 10^{-24} \text{ m}^2 \text{ s}^{-1}$ and the grain boundary diffusion parameter $P = 1.9 \times 10^{-25} \text{ m}^3 \text{ s}^{-1}$ for Co in W at a temperature of 1100 K are used [51]. Assuming a grain boundary thickness of $\delta = 5 \text{ \AA}$ yields the grain boundary diffusion coefficient $D_{gb} = P/\delta = 3.8 \times 10^{-14} \text{ m}^2 \text{ s}^{-1}$. For a sample with a surface area A_s of 1 cm^2 and cubic grains, the total area of the grain boundaries A_{gb} can be calculated: this calculation yields $A_{gb}^{200 \text{ nm}} = 5 \times 10^{-7} \text{ m}^2$ or $A_{gb}^{4 \mu\text{m}} = 0.3 \times 10^{-7} \text{ m}^2$ for a grain size of 200 nm as found in this study and a grain size of 4 μm as found for W in ref. [11], respectively. Thus, A_{gb} depends on the grain size. As the total flux Φ_{gb} through the grain boundaries is proportional to $D_{gb} \times A_{gb}$, the flux through the grain boundaries is expected to be higher with smaller grains. Further, the contribution of the volume diffusion can be estimated by

$$\frac{D_V A_s}{D_{gb} A_{gb}} = 10^{-6}. \quad (5)$$

Thus, the diffusion is dominated by grain boundary diffusion and smaller grains yield an increase in the total diffusion flux of particles proportional to A_{gb} . However, this microstructure on its own is not sufficient for the material to form a protective Cr_2O_3 layer as seen in the binary W-Cr alloy in Figure 4d. The addition of yttria is crucial.

6. Investigations on a Nano-Scale

6.1. Results of a Scanning Transmission Electron Microscopy Study

Parts of this study are briefly introduced in ref. [17]. Here we provide a detailed assessment. As discussed previously, the alloy should be in the second oxidation stage as long as there are elevated temperatures in the power plant. Therefore, the behavior in this stage is of key interest and the W-12Cr-0.5Y sample shown in Figure 4b is selected for STEM measurement to have a nano-scale insight into the material. A lamella, sketched in Figure 8a, with a thickness of $\sim 0.08 \mu\text{m}$, a width of $\sim 11 \mu\text{m}$, and a height of $\sim 8.6 \mu\text{m}$ is prepared by FIB. It is cut perpendicular to the substrate, thus the layered structure of oxide and alloy remain.

Imaging of the lamella is performed by STEM and EDX with an acceleration voltage of 200 kV. Due to the finite thickness of $\sim 0.08 \mu\text{m}$, it is possible that features overlap in viewing direction, as illustrated in the schematic in Figure 8a. Thus, in the 2D-image a superposition of structures is possible. The aim is understanding the distribution of elements within the structure on a nano-scale, in particular to also resolve Y.

The bottom half of the sample, region A in Figure 8a, is shown in Figure 8b–d. The electron image, Figure 8b, exhibits a regular pattern, indicating a variation of concentration parallel to the surface. The periodicity of 7 nm correlates to the rotation speed of the stage in the magnetron, during every turn of the stage $\sim 7 \text{ nm}$ of material are deposited. Further, grain boundaries and grains with different contrast are shown in Figure 8. The information obtained in the EDX-measurement, Figure 8c, prove that the three bright spots have a higher Cr content than the other grains. Consequently the other grains are referred as Cr-poor phase. The spectrum in the inset of Figure 8d shows a peak at the $K_{\alpha 1}$ -line of Y. This peak proves that Y is detected. The mapping, Figure 8d, shows atomically dispersed yttria within the observed region, no yttria particles are resolved.

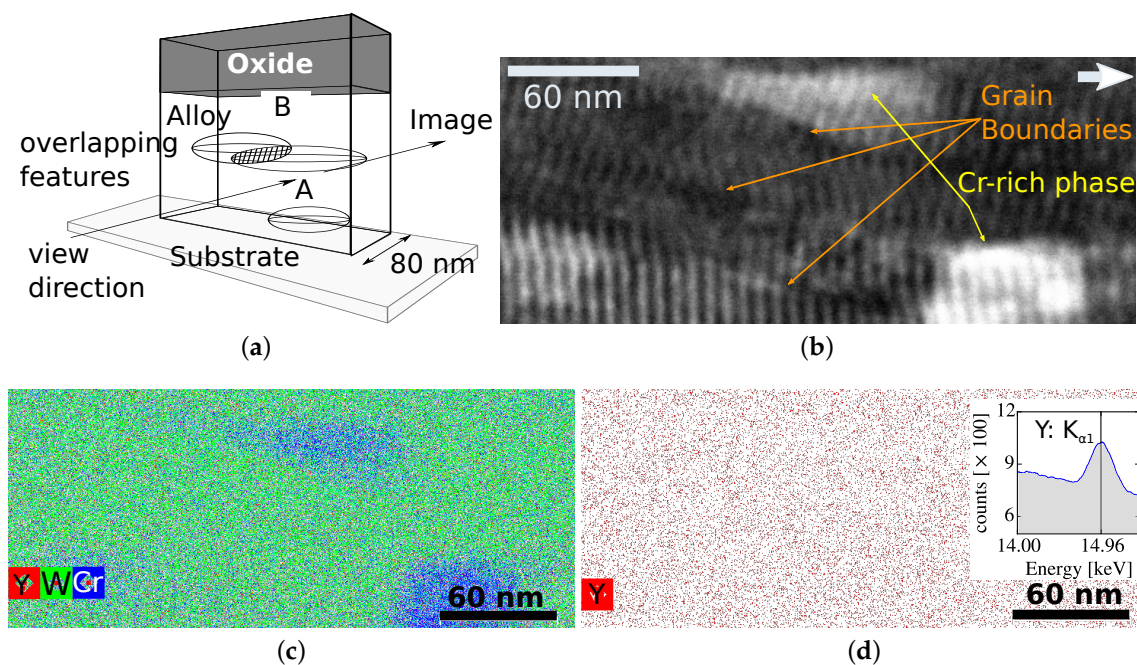


Figure 8. (a) Schematic drawing of the lamella, not in scale. A, and B mark regions where measurements are conducted; (b) STEM measurement in region A from (a). The alloy W-12Cr-0.5Y is oxidized at a temperature of 1273 K at 20 kPa O_2 and 80 kPa Ar partial pressure for 75 min. The white arrow on top right points towards the surface oxide layer; (c) EDX measurement map of tungsten, chromium, and yttrium overlaid; (d) EDX measurement map of yttrium and the spectrum added up over the whole mapping area in the inset.

The interface between the alloy and the surface oxide layer, region B in Figure 8a, is shown in Figure 9. In the electron image, Figure 9a, there is a large brightness deviation between the surface oxide layer and the alloy: two different color scales are used to have good contrast. In EDX all contained elements (W, Cr, Y, and O) indicate a sharp composition change at the interface. In the surface layer, where only small variations in contrast are visible in the electron image, a strong Cr and O signal is measured, whereas no W or Y is detected. That indicates a pure Cr_2O_3 surface layer. In the alloy, a strong W signal is detected, only the brighter spots in the electron image have slightly reduced intensity. These spots exhibit increased Cr and O signal, which is low elsewhere in the alloy. Thus, the bright spots correspond to internal oxidation of Cr. Y, Figure 9e, shows a fairly homogenous signal within the alloy, no dependence on grains is detected. Right at the interface an yttria enriched, circular spot with a diameter of about 30 nm is detected.

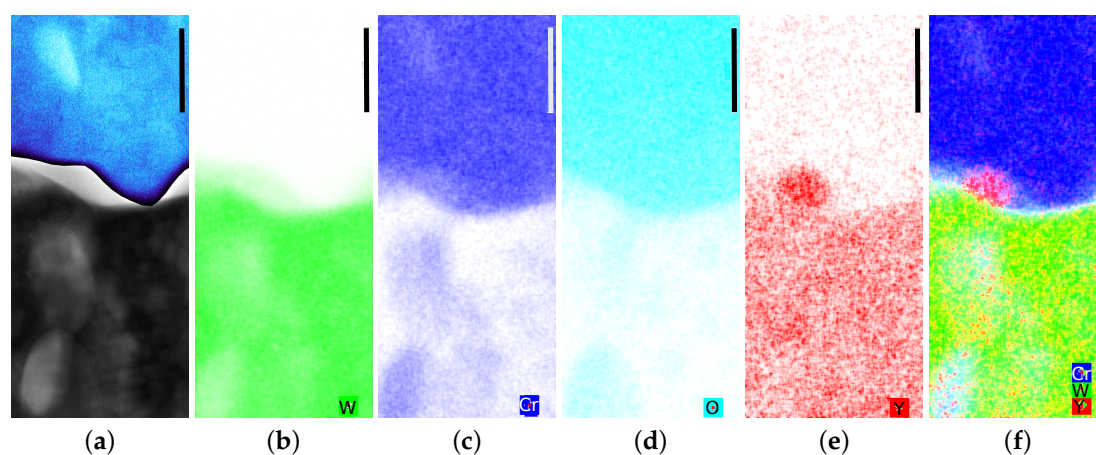


Figure 9. STEM measurement in region B from Figure 8a. The alloy W-12Cr-0.5Y is oxidized at a temperature of 1273 K at 20 kPa O_2 and 80 kPa Ar partial pressure for 75 min. The scale-bar in the top right corner has a length of 50 nm for all images. (a) Electron image using two different color maps: One for the Cr_2O_3 layer and one for the alloy; EDX map measurements of (b) tungsten; (c) chromium; (d) oxygen; and (e) yttrium; (f) Overlay of images (b,c,e). These data were already briefly introduced in ref. [17].

6.2. Importance of Nano-Scale Effects for Understanding the Oxidation Resistance

The layered structure with a periodicity of 7 nm, caused by the rotation of the stage in the magnetron, indicates small periodic concentration gradients in the alloy. As the gradients are less pronounced near the interface, see Figure 9, where most of the diffusion occurs. Diffusion processes reduce the initial concentration gradients. However, the influence of the gradients on the diffusion and oxidation process is not clear. We expect only a minor influence, as the gradients are parallel to the surface. Thus, the knowledge gained here can be transferred to alloys obtained via other production routes.

The role of yttria can be partially understood by the STEM measurements shown in Figures 8 and 9. The first key observation on yttria is the presence of a few yttria-enriched circular spots with diameters around 30 nm, Figure 9. The yttria content in these spots is only a few percent higher compared to the yttria content in the W matrix, thus they cannot account for the contrast in the electron image. Still, they are a strong indication that yttria can provide additional nucleation sites for oxide growth. Nucleation sites can promote the selective oxidation of Cr for the protective oxide layer, thereby suppressing the oxidation of W: yttria particles can react with Cr_2O_3 to form YCrO_3 . The standard Gibbs energy of this reaction is $-2 \times 10^2 \text{ kJ mol}^{-1}$. Due to a high oxygen vacancy concentration, the compounds mentioned above offer a fast diffusion path for oxygen while blocking cation diffusion [33].

Another observation from the STEM measurements is that the internal oxide and the surface oxide layer hardly contain any W or Y. Thus, Cr must diffuse to form these features. The absence of yttria in the oxides raises a new question: how can yttria improve the protection performance of the surface Cr_2O_3 layer without being present in the Cr_2O_3 layer? There are two possible explanations. The first is that there is still yttria in the oxide layer, but below the detection limit. The second is that yttria only influences the formation process from the W matrix. Partial experimental support for the second hypothesis is to be found in the nucleation sites, Figure 9, and the suppression of pore-formation, shown in Figure 4.

Different hypotheses that can explain the improved oxidation resistance in the presence of yttria are possible:

- The nucleation sites are crucial for the improved oxidation resistance, as discussed above.
- The atomic dispersion of yttria changes the diffusion coefficients of Cr, O, and W: at one selected spot on the lamella, Figure 8, multiple grain boundaries are visible in the electron image. Research has shown yttria segregation at the grain boundaries [28]. However, here yttria is homogeneously distributed within the W matrix at atomic level. In the absence of diffusion data of yttria in W, we calculated using the data from metallic Y: the diffusion coefficient D of Y in W is given in analogy to Equation (3) with the pre-exponential factor $D_0 = 6.7 \times 10^{-7} \text{ m}^2\text{s}^{-1}$, and the diffusion energy $Q = 2.953 \text{ eV}$ valid in the temperature range from 1473 K to 1873 K [52]. Therefore, the displacement of metallic Y atoms by diffusion during the oxidation time of 75 min would be of the same order of magnitude as the typical grain size of the alloy. However, the Y is bound to oxygen. The bond length of each bond is 2.3 \AA [53], whereas the atomic radius of an Y^{3+} ion is only 0.9 \AA [45]. Thus, Y_2O_3 is very immobile and the atomic dispersion of the yttria, originating from atomic deposition in the magnetron, is stable throughout the oxidation experiment. This dispersion can change the diffusion coefficients of Cr, O, and W.

Most likely there is more than one mechanism making the Y such an effective active element: a closed protective oxide should form as fast as possible and adherence of the oxide is crucial to achieve oxidation resistance. The extremely rapid oxidation of pure W, Figure 3b, and the oxidation behavior of W-Cr underline the achieved improvement. The pores and the layered structure of the binary alloy after oxidation (Figure 4d) suggest major changes compared to the W-Cr-Y system. The surface Cr_2O_3 layer of the ternary alloy appears to be a much better diffusion barrier for O than the surface layer of the binary alloy: there is less internal oxidation in the ternary alloy and W cannot oxidize below the oxide layer of the ternary alloy. Another important finding from the layered structure of binary W-Cr is the local minimum in the Cr profile, Figure 4d. Cr is not capable to retain a homogeneous concentration along the depth of the alloy, a continuous Cr supply to the surface is not possible. A larger Cr reservoir in a thicker, binary alloy is not available for the passivation process. In contrast, in a ternary W-Cr-Y alloy the full Cr reservoir is available for the passivation process.

7. Conclusions and Outlook

W is the main candidate for plasma-facing armor material for future fusion power plants. However, air ingress in a LOCA causes formation and sublimation of radioactive WO_3 . This sublimation is a severe safety hazard. Therefore, studies on oxidation resistant W-(11-13)Cr-(0-1)Y alloys are conducted. The alloys studied in this paper are thin films with a thickness of $3 \mu\text{m}$ to $8 \mu\text{m}$ prepared by magnetron sputtering. The major findings are as follows:

1. A protective oxide layer forms which suppresses sublimation. Failure of the protective layer occurs in case of Cr depletion by W breaking through the protective oxide layer. Interpolation of the presented data predicts that the W-12Cr-0.5Y alloy can withstand a LOCA exposing the material to dry, O_2 -containing atmosphere at 1273 K.

2. Cr continuously diffuses to the outermost surface of the oxide, expanding freely and forming new protective oxides. Due to free expansion, stresses that could cause spallation are avoided.
3. Passivation can work, even after the formation of (α W, Cr) and (α Cr, W) phases on a nm-scale. Cr is continuously replenished from the bulk of the sample, including the (α Cr, W) phase, to the surface.
4. Yttria is homogeneously distributed within the W matrix and enriched in nucleation sites at the interface between oxide and metal. This distribution is different from the classical anticipation of Y distribution in localized areas in most cases in between the grains [33]. Yttria significantly improves the oxidation resistance as binary W-11Cr samples break within minutes at 1273 K.

Recent research has shifted to bulk alloys to have a larger material reservoir to achieve oxidation resistance for times relevant for application in a fusion power plant and to demonstrate long-term oxidation resistance. Further, the full potential of the new W-Cr-Y alloys should be tested by increasing the temperature, and by adding humidity to the atmosphere. The bulk alloys can also be used to investigate mechanical properties, such as the ductility, of the new W-Cr-Y alloys. Another project is modeling for an improved understanding of durability, transport, and stability of smart alloys.

Based on this improved understanding, a significant step towards the goal to develop an oxidation resistant W alloy is made. After further optimization, the full potential of W for high temperature application could be employed. These results can be of relevance for research and application outside the context of nuclear fusion energy, like for example the next generation of receivers for concentrated solar power stations [54].

Author Contributions: The contributions of the different authors can be classified by the Contributor Roles Taxonomy (CRediT): Conceptualization: F.K., T.W., A.L., C.L. and J.W.C.; Methodology: F.K., T.W., A.L., M.R., H.D. and U.B.; Formal Analysis: F.K., T.W., M.R., H.D. and U.B.; Investigation: F.K., T.W., M.R., X.Y.T., H.D. and U.B.; Resources: F.K., A.L., M.R., C.L., J.W.C., J.M. and U.B.; Data Curation: F.K., T.W., M.R., H. Du and U.B.; Writing—Original Draft Preparation: F.K.; Writing—Review & Editing: F.K., T.W., A.L., X.Y.T., J.S. and C.L.; Visualization: F.K.; Supervision: T.W., A.L., C.L., J.W.C. and J.M.; Project Administration: A.L., C.L., J.W.C. and J.M.; Funding Acquisition: A.L., C.L. and J.W.C.;

Funding: A part of this work has been carried out within the framework of the EUROfusion Consortium and has received funding from the Euratom research and training programme 2014–2018 under grant agreement No. 633053. The views and opinions expressed herein do not necessarily reflect those of the European Commission.

Conflicts of Interest: The authors declare no conflict of interest.

References

1. Shultis, J.; Faw, R. *Fundamentals of Nuclear Science and Engineering*; CRC Press: Boca Raton, FL, USA, 2002.
2. Yu, I.; Bazylev, B.; Landman, I.; Fetzer, R. *Design Strategy for the PFC in DEMO Reactor*; KIT Scientific Publishing: Karlsruhe, Germany, 2013; Volume 7637. [\[CrossRef\]](#)
3. Maisonnier, D.; Cook, I.; Sardain, P.; Boccaccini, L.; Bogusch, E.; Broden, K.; Di Pace, L.; Forrest, R.; Giancarli, L.; Hermsmeyer, S.; et al. The European power plant conceptual study. *Fusion Eng. Des.* **2005**, *75*, 1173–1179. [\[CrossRef\]](#)
4. Lukac, F.; Vilemova, M.; Nevrla, B.; Klecka, J.; Chraska, T.; Molnarova, O. Properties of Mechanically Alloyed W-Ti Materials with Dual Phase Particle Dispersion. *Metals* **2017**, *7*, 3. [\[CrossRef\]](#)
5. Koch, F.; Brinkmann, J.; Lindig, S.; Mishra, T.P.; Linsmeier, C. Oxidation behaviour of silicon-free tungsten alloys for use as the first wall material. *Phys. Scr.* **2011**, *T145*, 014019. [\[CrossRef\]](#)
6. Linsmeier, C.; Rieth, M.; Aktaa, J.; Chikada, T.; Hoffmann, A.; Hoffmann, J.; Houben, A.; Kurishita, H.; Jin, X.; Li, M.; et al. Development of advanced high heat flux and plasma-facing materials. *Nucl. Fusion* **2017**, *57*, 092007. [\[CrossRef\]](#)
7. Coenen, J.W.; Antusch, S.; Aumann, M.; Biel, W.; Du, J.; Engels, J.; Heuer, S.; Houben, A.; Hoeschen, T.; Jasper, B.; et al. Materials for DEMO and reactor applications - boundary conditions and new concepts. *Phys. Scr.* **2016**, *T167*, 014002. [\[CrossRef\]](#)
8. Ueda, Y.; Schmid, K.; Balden, M.; Coenen, J.W.; Loewenhoff, T.; Ito, A.; Hasegawa, A.; Hardie, C.; Porton, M.; Gilbert, M. Baseline high heat flux and plasma facing materials for fusion. *Nucl. Fusion* **2017**, *57*, 092006. [\[CrossRef\]](#)

9. Gilbert, M.R.; Sublet, J.C.; Forrest, R.A. *Handbook of Activation, Transmutation, and Radiation Damage Properties of the Elements Simulated Using FISPACT-II & TENDL*; Culham Center For Fusion Energy: Abingdon, UK, 2015.
10. Gilbert, M.R.; Eade, T.; Bachmann, C.; Fischer, U.; Taylor, N.P. Activation, decay heat, and waste classification studies of the European DEMO concept. *Nucl. Fusion* **2017**, *57*, 046015. [[CrossRef](#)]
11. Zhang, L.; Jiang, Y.; Fang, Q.; Liu, R.; Xie, Z.; Zhang, T.; Wang, X.; Liu, C. Comparative Investigation of Tungsten Fibre Nets Reinforced Tungsten Composite Fabricated by Three Different Methods. *Metals* **2017**, *7*, 249. [[CrossRef](#)]
12. Rieth, M.; Dudarev, S.; de Vicente, S.G.; Aktaa, J.; Ahlgren, T.; Antusch, S.; Armstrong, D.; Balden, M.; Baluc, N.; Barthe, M.F. A brief summary of the progress on the EFDA tungsten materials program. *J. Nucl. Mater.* **2013**, *442*, 173–180. [[CrossRef](#)]
13. Coenen, J.W.; Mao, Y.; Almanstötterg, J.; Calvo, A.; Sistla, S.; Gietl, H.; Jasper, B.; Riesch, J.; Rieth, M.; Pintsuk, G.; et al. Advanced Materials for a Damage Resilient Divertor Concept for DEMO. *Fusion Eng. Des.* **2017**, *124*, 964–968. [[CrossRef](#)]
14. Jasper, B.; Schoenen, S.; Du, J.; Hoeschen, T.; Koch, F.; Linsmeier, C.; Neu, R.; Riesch, J.; Terra, A.; Coenen, J.W. Behavior of tungsten fiber-reinforced tungsten based on single fiber push-out study. *Nucl. Mater. Energy* **2016**, *9*, 416. [[CrossRef](#)]
15. Brandes, E.; Brook, G.; Paufler, P. (Eds.) *Smithells Metals Reference Book*; Butterworth-Heinemann: Oxford, UK, 1992.
16. Wegener, T.; Klein, F.; Litnovsky, A.; Rasinski, M.; Brinkmann, J.; Koch, F.; Linsmeier, C. Development of yttrium-containing self-passivating tungsten alloys for future fusion power plants. *Nucl. Mater. Energy* **2016**, *9*, 394–398. [[CrossRef](#)]
17. Litnovsky, A.; Wegener, T.; Klein, F.; Linsmeier, C.; Rasinski, M.; Kreter, A.; Unterberg, B.; Coenen, J.W.; Du, H.; Mayer, J.; et al. Smart tungsten alloys as a material for the first wall of a future fusion power plant. *Nucl. Fusion* **2017**, *57*, 066020. [[CrossRef](#)]
18. Litnovsky, A.; Wegener, T.; Klein, F.; Linsmeier, C.; Rasinski, M.; Kreter, A.; Unterberg, B.; Vogel, M.; Kraus, S.; Breuer, U.; et al. Smart alloys for a future fusion power plant: First studies under stationary plasma load and in accidental conditions. *Nucl. Mater. Energy* **2016**, *12*, 1363–1367. [[CrossRef](#)]
19. Eckstein, W. *Sputtering by Particle Bombardment: Experiments and Computer Calculations from Threshold to MeV Energies*; Chapter Sputtering Yields; Springer: Berlin/Heidelberg, Germany, 2007; pp. 33–187. [[CrossRef](#)]
20. Litnovsky, A.; Wegener, T.; Klein, F.; Linsmeier, C.; Rasinski, M.; Kreter, A.; Tan, X.Y.; Schmitz, J.; Mao, Y.; Coenen, J.W.; et al. Advanced smart tungsten alloys for a future fusion power plant. *Plasma Phys. Control. Fusion* **2017**, *59*, 064003. [[CrossRef](#)]
21. Wallwork, G.R.; Hed, A.Z. Some limiting factors in the use of alloys at high temperatures. *Oxid. Met.* **1971**, *3*, 171–184. [[CrossRef](#)]
22. Koch, F.; Bolt, H. Self passivating W-based alloys as plasma facing material for nuclear fusion. *Phys. Scr.* **2007**, *T128*, 100–105. [[CrossRef](#)]
23. Telu, S.; Mitra, R.; Pabi, S.K. Effect of Y₂O₃ Addition on Oxidation Behavior of W-Cr Alloys. *Metall. Trans.* **2015**, *46*, 5909–5919. [[CrossRef](#)]
24. Birks, N.; Meier, G.; Pettit, F. *Introduction to the High-Temperature Oxidation of Metals*; Cambridge University Press: Cambridge, UK, 2006.
25. Griffiths, W.T.; Pfeil, L. Improvements in Heat Resistant Alloys. U.K. Patent No. 459848, 1937.
26. Lang, E. (Ed.) *The Role of Active Elements in the Oxidation Behaviour of High Temperature Metals and Alloys*; Elsevier Applied Science: London, UK, 1989.
27. Buerge, R.; Maier, H.J.; Niendorf, T. *Handbuch Hochtemperatur-Werkstofftechnik*; PRAXIS: Chichester, UK, 2011.
28. Przybylski, K.; Garratt-Reed, A.J.; Yurek, G.J. Grain Boundary Segregation of Yttrium in Chromia Scales. *J. Electrochem. Soc.* **1988**, *135*, 509–517. [[CrossRef](#)]
29. Stringer, J.; Wilcox, B.A.; Jaffee, R.I. The high-temperature oxidation of nickel-20 wt. % chromium alloys containing dispersed oxide phases. *Oxid. Met.* **1972**, *5*, 11–47. [[CrossRef](#)]
30. Quadackers, W.J.; Holzbrecher, H.; Briefs, K.; Beske, H. The Effect of Ytria Dispersions on the Growth Mechanisms and Morphology of Chromia and Alumina Scales. In *The Role of Active Elements in the Oxidation Behaviour of High Temperature Metals and Alloys*; Lang, E., Ed.; Springer: Dordrecht, The Netherlands, 1989; pp. 155–173. [[CrossRef](#)]
31. Mevrel, R. Cyclic oxidation of high-temperature alloys. *J. Mater. Sci. Technol.* **1987**, *3*, 531–535. [[CrossRef](#)]

32. Tang, Q.; Sun, H.; Zhou, M.; Quan, G. Effect of Y Addition on the Semi-Solid Microstructure Evolution and the Coarsening Kinetics of SIMA AZ80 Magnesium Alloy. *Metals* **2017**, *7*, 416. [[CrossRef](#)]
33. Saito, Y.; Önay, B.; Maruyama, T. The reactive element effect (REE) in oxidation of alloys. *J. Phys. IV* **1993**, *3*, 217–230. [[CrossRef](#)]
34. Stroosnijder, M.; Sunderkijtter, J.D.; Cristobal, M.J.; Jenett, H.; Isenbügel, K.; Baker, M.A. The influence of yttrium ion implantation on the oxidation behaviour of powder metallurgically produced chromium. *Surf. Coat. Technol.* **1996**, *83*, 205–211. [[CrossRef](#)]
35. Wegener, T.; Klein, F.; Litnovsky, A.; Rasinski, M.; Brinkmann, J.; Koch, F.; Linsmeier, C. Development and analyses of self-passivating tungsten alloys for DEMO accidental conditions. *Fusion Eng. Des.* **2017**, *124*, 183–186. [[CrossRef](#)]
36. Schmitz, J.; Litnovsky, A.; Klein, F.; Wegener, T.; Tan, X.Y.; Rasinski, M.; Mutzke, A.; Hansen, P.; Kreter, A.; Pospieszczyk, A.; et al. WCrY smart alloys as advanced plasma-facing materials—Exposure to steady-state pure deuterium plasmas in PSI-2. *Nucl. Mater. Energy* **2018**, In Press. [[CrossRef](#)]
37. Ernst Ruska-Centre for Microscopy and Spectroscopy with Electrons. FEI Titan 80-300 STEM. *JLSRF* **2016**, *2*. [[CrossRef](#)]
38. Turkdogan, E. *Physical Chemistry of High Temperature Technology*; Academic Press: New York, NY, USA, 1980.
39. Calvo, A.; Ordas, N.; Iturriza, I.; Pastor, J.Y.; Tejado, E.; Palacios, T.; Garcia-Rosales, C. Manufacturing of self-passivating tungsten based alloys by different powder metallurgical routes. *Phys. Scr.* **2016**, *T167*, 014041. [[CrossRef](#)]
40. Swanson, H.E. *Standard X-ray Diffraction Powder Patterns*; National Bureau of Standards: Washington, DC, USA, 1953; Volume 1, p. 28.
41. Thornton, J.A. Influence of substrate temperature and deposition rate on structure of thick sputtered Cu coatings. *J. Vac. Sci. Technol.* **1975**, *12*, 830. [[CrossRef](#)]
42. Ross, R.G.; Hume-Rothery, W. High temperature X-ray metallography: I. A new debye-scherrer camera for use at very high temperatures II. A new para-focusing camera III. Applications to the study of chromium, hafnium, molybdenum, rhodium, ruthenium and tungsten. *J. Less-Common Met.* **1963**, *5*, 258–270. [[CrossRef](#)]
43. Reed, T.B. (Ed.) *Free Energy of Formation of Binary Compounds*; MIT Press: Cambridge, MA, USA, 1971.
44. Royer, L.; Ledoux, X.; Mathieu, S.; Steinmetz, P. On the Oxidation and Nitridation of Chromium at 1300 C. *Oxid. Met.* **2010**, *74*, 79–92. [[CrossRef](#)]
45. Shannon, R.D. Revised effective ionic radii and systematic studies of interatomic distances in halides and chalcogenides. *Acta Crystallogr. Sect. A* **1976**, *32*, 751–767. [[CrossRef](#)]
46. Litnovsky, A.; Wegener, T.; Klein, F.; Linsmeier, C.; Rasinski, M.; Kreter, A.; Tan, X.Y.; Schmitz, J.; Coenen, J.W.; Mao, Y.; et al. New oxidation-resistant tungsten alloys for use in the nuclear fusion reactors. *Phys. Scr.* **2017**, *T170*, 014012. [[CrossRef](#)]
47. Rosman, K.J.R.; Taylor, P.D.P. Isotopic compositions of the elements 1997. *Pure Appl. Chem.* **1998**, *70*, 217–235. [[CrossRef](#)]
48. Thompson, A.C.; Attwood, D.T.; Gullikson, E.M.; Howells, M.R.; Kortright, J.B.; Robinson, A.L.; Underwood, J.H.; Kim, K.; Kirz, J.; Lindau, I.; et al. *X-ray Data Booklet*; Center for X-ray Optics and Advanced Light Source; Lawrence Berkeley National Laboratory: Berkeley, CA, USA, 2001.
49. Andersen, C.A. Progress in analytic methods for the ion microprobe mass analyzer. *Int. J. Mass Spectrom. Ion Phys.* **1969**, *2*, 61. [[CrossRef](#)]
50. Klotsman, S.M.; Koloskov, V.; Osetrov, S.; Polikarpova, I.; Tatarinova, G.; Timofeev, A. Chromium and molybdenum diffusion in tungsten single crystals. *Fiz. Met. Metalloved.* **1989**, *67*, 767–774.
51. Lee, J.; Klockgeter, K.; Herzig, C. Grain boundary self and impurity diffusion in Tungsten in the Temperature range of activated sintering. *J. Phys. Colloq.* **1990**, *51*, 569–574. [[CrossRef](#)]
52. Gornyy, D.; Altovskiy, R. Diffusion of Yt in refractory metals. *Fiz. Met. Metalloved.* **1971**, *31*, 781.

53. Lazdins, K.; Kuzmin, A. Local structure and lattice dynamics of cubic Y_2O_3 : An X-ray absorption spectroscopy study. In Proceedings of the OP Conference Series: Materials Science and Engineering, St George, UT, USA, 6–10 November 2017; Volume 77. [[CrossRef](#)]
54. Zhu, G.; Libby, C. Review and Future Perspective of Central Receiver Design and Performance. *AIP Conf. Proc.* **2017**, *1850*. [[CrossRef](#)]



© 2018 by the authors. Licensee MDPI, Basel, Switzerland. This article is an open access article distributed under the terms and conditions of the Creative Commons Attribution (CC BY) license (<http://creativecommons.org/licenses/by/4.0/>).